5.1.2 EXPERIMENTAL CHARACTERIZATION IN THE P-E DOMAIN

The ferroelectric capacitor follows the dynamics (4.8) in the *P-E* domain. This model describes the hysteretic behavior of the ferroelectric capacitor. Before proceeding to the main point i.e. the detection of target E-fields, the material parameters *(a,b,c,τ)* must be determined. This has been performed by driving the device by an AC electric field at various frequencies and amplitudes, and acquiring the output voltage *V_{out}* of the Sawyer-Tower circuit. No (other) external electric field is present. The driving AC electric field must be suprathreshold, i.e. of sufficient amplitude to cause the system to sweep through its hysteresis loop or, equivalently, switch between the two stable states in the potential of Figure 4-1, on a timescale controlled by the driving period. Clearly, the driving field must be of sufficient amplitude and frequency to overcome the coercive field of the material, in a real system. Here it is important to note that, from a theoretical standpoint, one can compute the deterministic switching threshold of the dynamics (4.8) via a simple calculation of the inflexion points of the potential energy function (4.7). For a static driving field, one obtains a value of $\left(\dfrac{4a^3}{27b}\right)^{1/2}$. With a

time-sinusoidal driving field, the corresponding threshold value of the driving amplitude scales as the 2/3 power of the driving frequency [163]. The evaluation of the model parameters starts by identifying *a*, *b*, *c* and *τ* at the highest frequency and amplitude of the driving. The Nelder-Mead optimization algorithm [161] to minimize the squared difference between the experimental and theoretical polarizations is, then, applied; at its core is the root mean square type functional *J* that computes (as a percentage) the residuals between the predicted (via the model) values and the observed values of the polarization, that we seek to minimize:

$$J\% = \frac{\sqrt{\sum(\hat{P}-P_{\exp})^2}}{\sum(P_{\exp})^2}\cdot 100 \tag{4.23}$$

Here, $\hat{P}$ represents the estimated polarization obtained via the evaluated parameters, and P_{exp} represents the experimental polarization obtained by inverting (4.4). To prevent convergence of the minimization algorithm to a local minimum point in any iteration, the constraint $P_r = \sqrt{(a/b)}$ is imposed on the parameters a and b; this relationship derives from the potential (4.7) representing the two stable states shown in Figure 4-1b, when no forcing field is present. Another convenience adopted for the same purpose has been to consider the parameters identified for a given frequency and amplitude of the driving voltage as initial conditions for the identification of parameters related to the driving having the same frequency but smaller amplitude and vice versa.

Figure 4-13 shows two examples of experimental and theoretical hysteresis loops for driving voltages having amplitudes of 10 V_{pp} and 50 V_{pp} and frequency 100 Hz, with 10 V_{pp} being the smallest value able to induce switching (between the two stable minima of the potential energy function) in the polarization. Table 4-1 summarizes the values of the parameters obtained through the minimization procedure for the case shown in Figure 4-13. All the model parameters have been, first, estimated with 50 V_{pp} @ 1 kHz driving to take into account the system dynamics, the time constant τ has been then fixed to this value while the other parameters have been used as initial values for the estimations performed in the other working conditions shown in Table 4-1. Characterization has been performed for a more spread set of voltages and frequencies, estimated parameters are not reported here for the sake of brevity. It can be observed that different values of the parameters a, b and c are obtained for different driving signal amplitudes, this being in line with earlier predictions [163] of delayed transitions in bistable systems under time-periodic external signals.

The aim of the previous analysis has been the understanding of the non linear behavior of the device. This is necessary for simulation purposes and for the estimation of the material parameters which allow us to quantify the potential barrier height which constraints the device response to external perturbations.
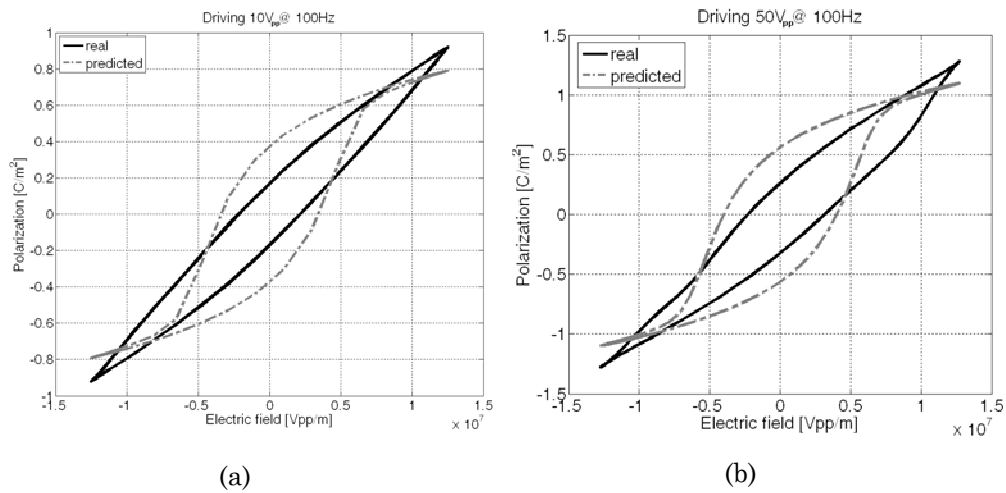
(a)   (b)

FIGURE 4-13   Experimental and theoretical (dashed line) hysteresis loops for driving voltages having amplitudes of (a) 10 V_{pp} and (b) 50 V_{pp} with frequency of 100 Hz.

TABLE 4-1   Model parameters derived by the Nelder-Mead optimization algorithm.

Frequency [Hz]	Parameter	Driving 10 [V]	Driving 50 [V]
100	a	0.745e-3	0.773e-3
	b $[C/m^2]^{-2}$	2.580e-2	1.144e-2
	c [F/m]	0.964e-9	1.255e-9
	τ [s]	2.407e-6	2.407e-6
	J%	19.053	18.865
	P_r $[C/m^2]$	0.17	0.26
1000	a	1.72e-2	1.75e-2
	b $[C/m^2]^{-2}$	7.287e-2	6.115e-2
	c [F/m]	5.985e-9	8.143e-9
	τ [s]	2.407e-6	2.407e-6
	J%	16.132	15.063
	P_r $[C/m^2]$	0.42	0.53

5.1.3   THE IDENTIFICATION TOOL

To the purpose to perform a model identification for the ferroelectric capacitors, a Matlab® tool has been developed.

Figure 4-14 shows the GUI of the identification tool. It permits the setting of required parameters such as the initial conditions for the optimization algorithm, the sampling frequency of the experimentally acquired signal to load and some circuital and geometric parameter such as the value of the feedback capacitor, the thickness of the ferroelectric layer and its surface area. These parameters are required to convert the loaded voltage signals in the polarization and electric field signals. Moreover it shows the experimental and the predicted hysteresis (by the model) together with the estimated parameters trend.
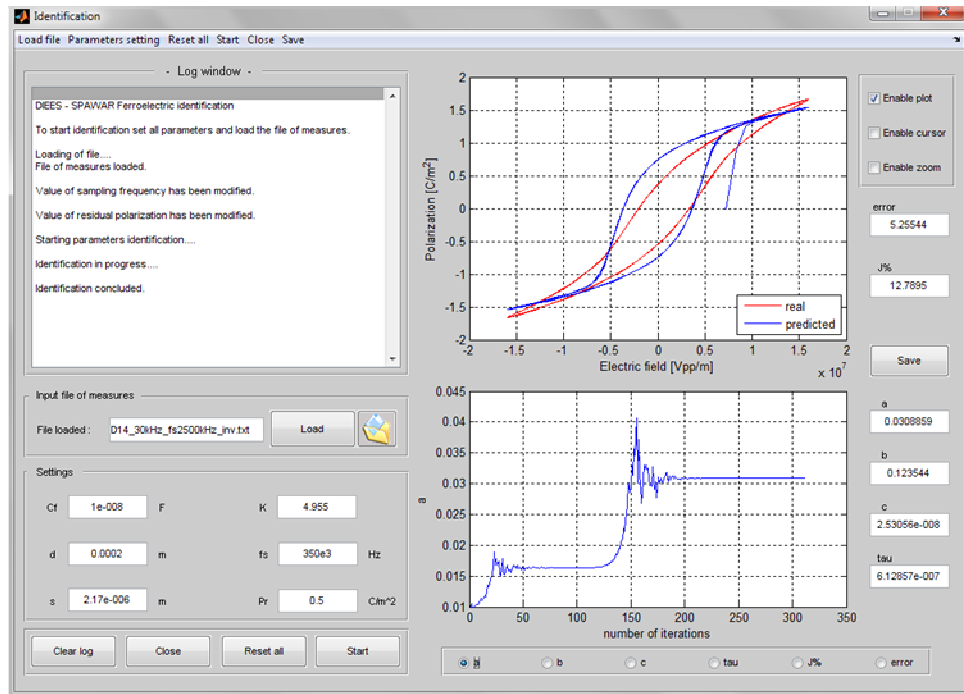

FIGURE 4-14   GUI of the identification tool.

The core of the tool consist in three main script named: "algoritmo.m", "funzione_errore.m", and "risoluzione-numerica.m", respectively.

In essence, the tool identifies a set of parameters for the analytical model (for example the parameters a, b, c, τ for the quartic potential model) chosen to represent the ferroelectric capacitor behavior by the Nelder-Mead optimization algorithm (a simplex search method).

After the loading of the Sawyer-Tower input-output signals and the plotting of the P-E hysteresis, the setting of the remnant polarization value is required. Then the identification algorithm starts by the Matlab *fminsearch* call: it finds the minimum of a scalar function of several variables (defined in the script "risoluzione_numerica.m"), starting at an initial estimate (the initial conditions previously defined). This is generally referred to as unconstrained nonlinear optimization. The optimization algorithm generally stops when a local minimum is reached, then it returns a set of model parameters.

The script "funzione_errore.m" defines the error function to minimize by searching an optimal set of parameters for the model defined in the third script "risoluzione_numerica.m". At every iteration it shows the model form with the estimated parameters together with the experimental hysteresis.

5.1.4 THE BEHAVIORAL PSPICE MODEL

In order to perform numerical simulations of the system, a circuital dynamic model has been developed for the ferroelectric capacitors. Excellent agreement has been achieved between our measurements and the corresponding circuit simulations. In particular, the circuital modeling of a ferroelectric capacitor through PSPICE has been developed using a behavioral representation. The method also optimizes the process of establishing the parameter values germane to a particular hysteresis loop.

Consider the model that schematizes the capacitor as a *"displacement current"* generator, shown in Figure 4-15a, driven by a voltage difference that can be derived from two fundamental equations. Models underpinning the device behavior can then be realized as follows:
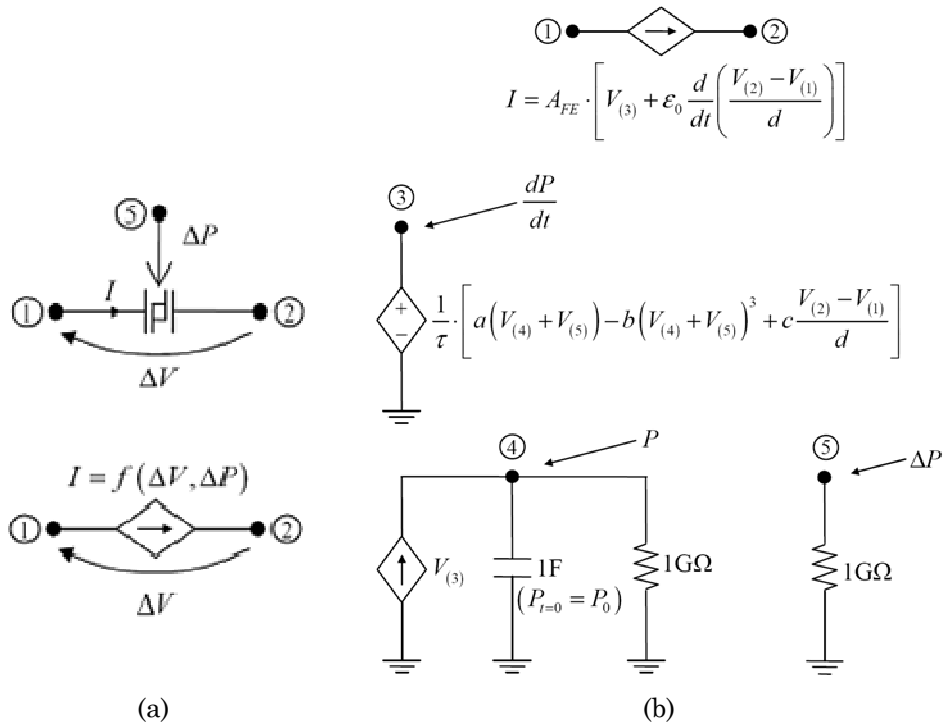
$$I = A_{FE} \cdot \left[V_{(3)} + \varepsilon_0 \frac{d}{dt} \left(\frac{V_{(2)} - V_{(1)}}{d} \right) \right]$$

$$\frac{1}{\tau} \cdot \left[a \left(V_{(4)} + V_{(5)} \right) - b \left(V_{(4)} + V_{(5)} \right)^3 + c \frac{V_{(2)} - V_{(1)}}{d} \right]$$

(a)   (b)

FIGURE 4-15   (a) Graphic representation of the spice model for the ferroelectric capacitor. (b) Spice implementation of the ferroelectric capacitor.

$$D = P + \varepsilon_0 E = \frac{Q}{A_{FE}} \tag{4.24}$$

where D, P and E are the normal components to the capacitor electrodes having area A_{FE} of the vectors for displacement, electric polarization, and electric field, respectively.

Rearranging equation (4.24), it is possible to derive

$$Q = A_{FE} (P + \varepsilon_0 E) \tag{4.25}$$

Deriving equation (4.25), an expression for the current can be obtained

$$I = \frac{dQ}{dt} = A_{FE} \left(\frac{dP}{dt} + \varepsilon_0 \frac{dE}{dt} \right) \tag{4.26}$$

which is our first "constitutive" equation. In the second equation we have to take into account the dynamic behavior of the ferroelectric material

$$\tau \frac{dP}{dt} = aP - bP^3 + cE \tag{4.27}$$

where a, b, c and τ are the model parameters and E is the electric field amplitude. The value of P can be recursively evaluated by (4.27)

$$P = \int \left(\frac{dP}{dt} \right) dt = \frac{1}{\tau} \int \left(aP - bP^3 + cE \right) dt \tag{4.28}$$

A parallel plate capacitor, with a plate separation d, has been considered to evaluate the electric field amplitude E

$$E = \frac{V(2) - V(1)}{d} \tag{4.29}$$

The previous model may also take into account an external perturbation, to the polarization of the ferroelectric capacitor, induced by the target field through the sensing electrode. An auxiliary input allows for introducing such a perturbation, where the voltage at this node (ΔP) is expressed in units (C/m^2) and summed to the actual value of P. Thus, we can write equation (4.27) as

$$\frac{dP}{dt} = \frac{1}{\tau} \left[a(P + \Delta P) - b(P + \Delta P)^3 + cE \right] \tag{4.30}$$

and as a consequence

$$P = \frac{1}{\tau} \int \left[a(P + \Delta P) - b(P + \Delta P)^3 + cE \right] \tag{4.31}$$

Hence, equation (4.30) models the representation of the PSPICE circuit displayed in Figure 4-15b.

The ferroelectric capacitor model (*FCAP_Pin*) can be included in a Sawyer-Tower configuration as shown in Figure 4-16a. A typical simulation result is shown in Figure 4-16b. In particular, two hysteresis loops are shown to highlight the device behavior in the absence (blue line and in the presence (red line) of a target electric field having a fre-
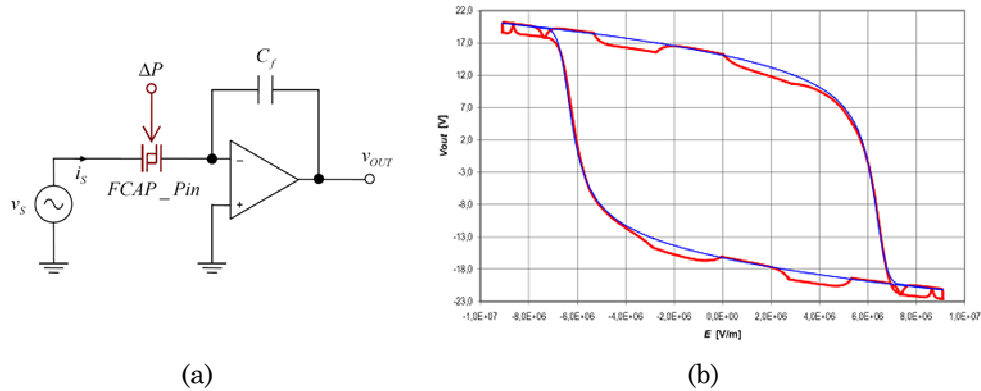
(a)   (b)

FIGURE 4-16   (a) Sawyer-Tower circuit simulated in the PSPICE environment; (b) Typical simulation results, highlighting the device behavior in the absence (blue line) and in the presence (red line) of a target electric field. A typical relationship between the target field and the perturbation ΔP has been adopted.

quency higher than the driving voltage.

5.1.5 RESPONSE TO AN EXTERNAL E-FIELD

Equation (4.13) relates the polarization of the ferroelectric material with the target electric field via the ratio of the surface areas of the charge collector and the sensing electrode. It asserts that a variation of the target electric field yields a proportional variation in the polarization state of the ferroelectric region under the sensing electrode and, hence, a variation of the output voltage of the conditioning circuit. This behavior is modeled by equation (4.14).

Figure 4-17a shows an example of polarization signal obtained by simulating (4.14) and (4.13) in Matlab® for a driving (i.e. reference) voltage of $10V_{pp}$@100 Hz and a target electric field of 14.29 V/m @ 10 Hz. The target electric field produces a "modulation" of the output signal whose depth depends on the intensity of the target field itself (Figure 4-17a): this is the information needed to estimate the target field. Actually the "modulation" depth also depends on the area of the charge collector (considering that the area of the sensing electrode is
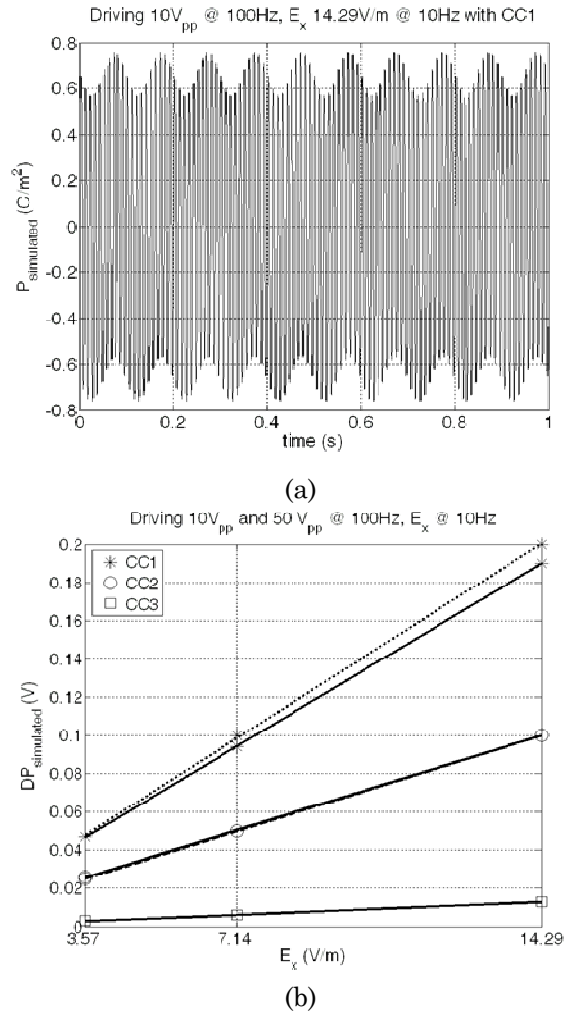
(a)

(b)

FIGURE 4-17   (a) An example of the polarization signal obtained by simulating (4.13) for a driving voltage of 10Vpp and considering a target electric field having amplitude 14.29 V/m @10Hz. The electric field produces a "modulation" (whose depth depends on the intensity of the target field) of the output signal. (b) Linear interpolation of the peak-to-peak modulation amplitude for three values of the target electric field with three different charge collectors (CC1, CC2 and CC3); the model predicts increasing device sensitivity with increasing size of the charge collector. The solid lines are for a driving voltage of 10 V_{pp}, while the dashed-lines are for a driving voltage of 50 V_{pp}.

constant) as stated by (4.13). Figure 4-17b shows the results obtained for three different values of the target electric field and with three different charge collectors having dimensions CC1: 30 cm x 39.5 cm, CC2: 25.5 cm x 25.5 cm and CC3: 9 cm x 9 cm, respectively.

The values estimated by simulation have been interpolated by a solid line (10 V_{pp}) and a dashed line (50 V_{pp}). It can be observed that the two sets of lines in Figure 4-17b are almost superimposed, therefore no significant improvements are obtained with an increase in the driving voltage. The relevant information derivable from this is that the model predicts an increase in the device sensitivity with an increase in size of the charge collector without a significant contribution from the larger driving voltage amplitude.

A further confirmation of the expected behavior can be obtained via the PSPICE model. The simulated model circuit with the ferroelectric capacitor is shown in Figure 4-18, while an example of the output voltage signal is shown in Figure 4-19. For the purpose of investigating the effect of the polarization ΔP, induced in the capacitance by the target E-field on the system output voltage, several simulations for different driving voltages and frequencies have been performed; in each case, we vary the amplitude and the frequency of the perturbation on the third electrode of the ferroelectric capacitance. The results confirm the expected behavior including the linear relationship between ΔP and the amplitude of the output voltage modulation, as shown in Figure 4-20 for two amplitudes of the driving voltage.
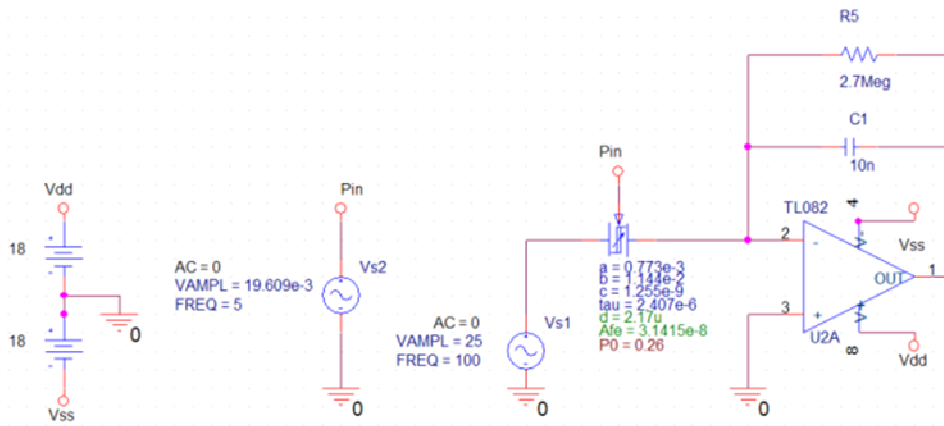
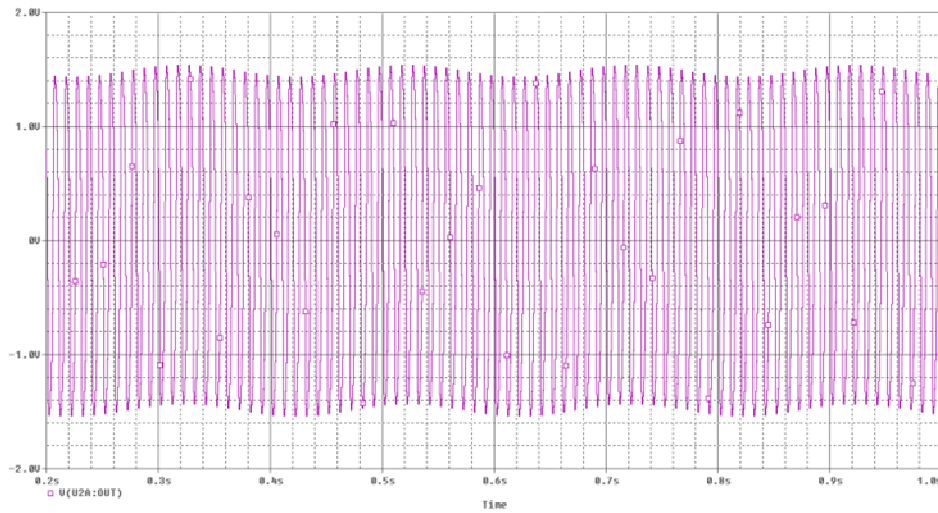**FIGURE 4-18**   The PSPICE model circuit with the ferroelectric capacitor.

FIGURE 4-19   An example of the output voltage signal of the PSPICE model in Figure 4-18 showing the effect of the perturbation on the third electrode of the ferroelectric capacitance
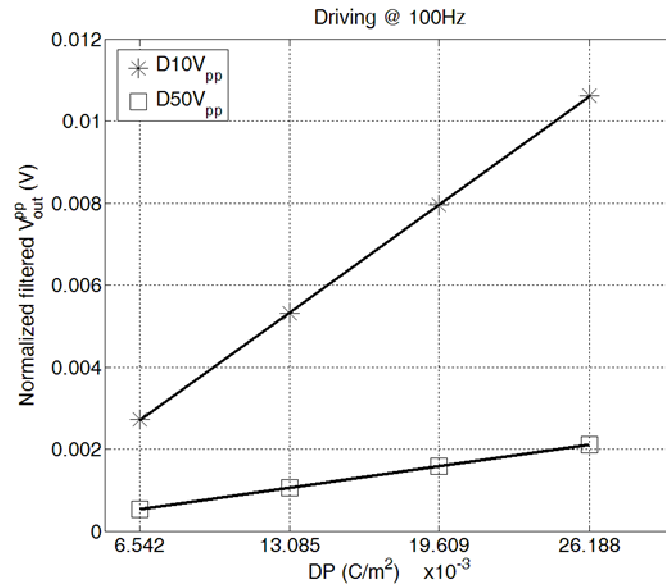
FIGURE 4-20   The linearity feature relating the V_{out} amplitude modulation with different ΔP.

5.1.6   EXPERIMENTAL RESULTS

The experimental setup shown in Figure 4-21 consists of two large sheet electrodes of 2 m x 2 m and a guard chamber to shield the sensor in order to avoid a direct (i.e., bypassing the charge collector) polarization of the ferroelectric. The two electrodes, separated by 1.40 m, are used to generate a uniform electric field. An AC voltage is applied to these parallel plates producing the target electric field which, in turn, produces a modulation (see Figure 4-22) of the output signal; as already seen, the modulation amplitude is proportional to the target field intensity. To evaluate this modulation amplitude, the waveforms from the ST circuit have been low-pass filtered.

The experiments involve subjecting the capacitor to a target E-field having different intensities and frequencies, while also varying the dimensions of the charge collector. Specifically, the voltage (producing the target E-field across the capacitor) applied to the electrodes has been varied in amplitude from 5 V_{pp} to 20 V_{pp} in steps of 5 V_{pp} and its

FIGURE 4-21   Experimental setup. The two large electrodes (2 m x 2 m each) and the guard chamber are shown in (a); the charge collector is visible in (b).

frequency varied from 5 Hz to 100 Hz. Treating the two large electrodes as a parallel plate capacitor, the target electric field amplitudes were 3.57 V/m, 7.14 V/m, 10.7 V/m and 14.29 V/m.

The driving voltage, applied directly to the capacitor plates, has amplitude ranging from 10 V_{pp} to 50 V_{pp} and frequencies of 100 Hz, 500 Hz and 1 kHz. All the experiments have been repeated with the three charge collectors, CC1, CC2 and CC3. Table 4-2 summarizes the settings used for the experiments. Then, as already described, the (external) target E-field induces a modulation of the output signal. Figure 4-22a and 4-22c show examples of the output signal, after removal of the mean value (this is necessary to make the low frequency components visible) obtained by a driving signal of 10 V_{pp} @ 100 Hz and a target electric field of 14.29 V/m @ 5 Hz and 10 Hz.

For an in depth understanding of the effect of the target E-field on the device polarization a spectral analysis of the ST output signals (correlated to the device polarization) has been carried out. Figures 4-23 (a) and (b) show the power spectral density (PSD) in the range (0 – 110 Hz) of the signals shown in Figures 4-22b and 4-22d. It is easy to detect the main peak at the frequency (100 Hz) of the driving signal and a smaller one at the frequency of the target field (5Hz in

Figure 4-23a and 10Hz in Figure 4-23b). Figures 4-23c and 4-23d show a magnification (i.e. a "zoom") of the power spectral densities in the range (0 - 30 Hz); it is clear that a stronger target signal enhances the height of these peaks in the PSD.

The intensity of the target electric field is then estimated by low-pass filtering the output voltage signal of Sawyer-Tower circuit; examples of such signals are reported in Figures 4-22b and 4-22d.

Taking into account equations (4.4) and (4.13), a relationship between the low-pass filtered ST output signal and the external target field E_x can be considered to have the following form

$$\Delta V_{out}^{pp} = \alpha \Delta E_x + \beta \qquad (4.32)$$

Considering the peak-to-peak values of the filtered signals shown in Figure 4-21b, and repeating the experiments with three charge collectors, the results shown in Figure 4-23 have been obtained for target electric fields with frequencies of 5 Hz and 10 Hz. A linear interpolation of the experimental observations leads to the parameters (α, β) reported in Table 4-3.

TABLE 4-2   Settings used in the characterization of the device with a target electric field.

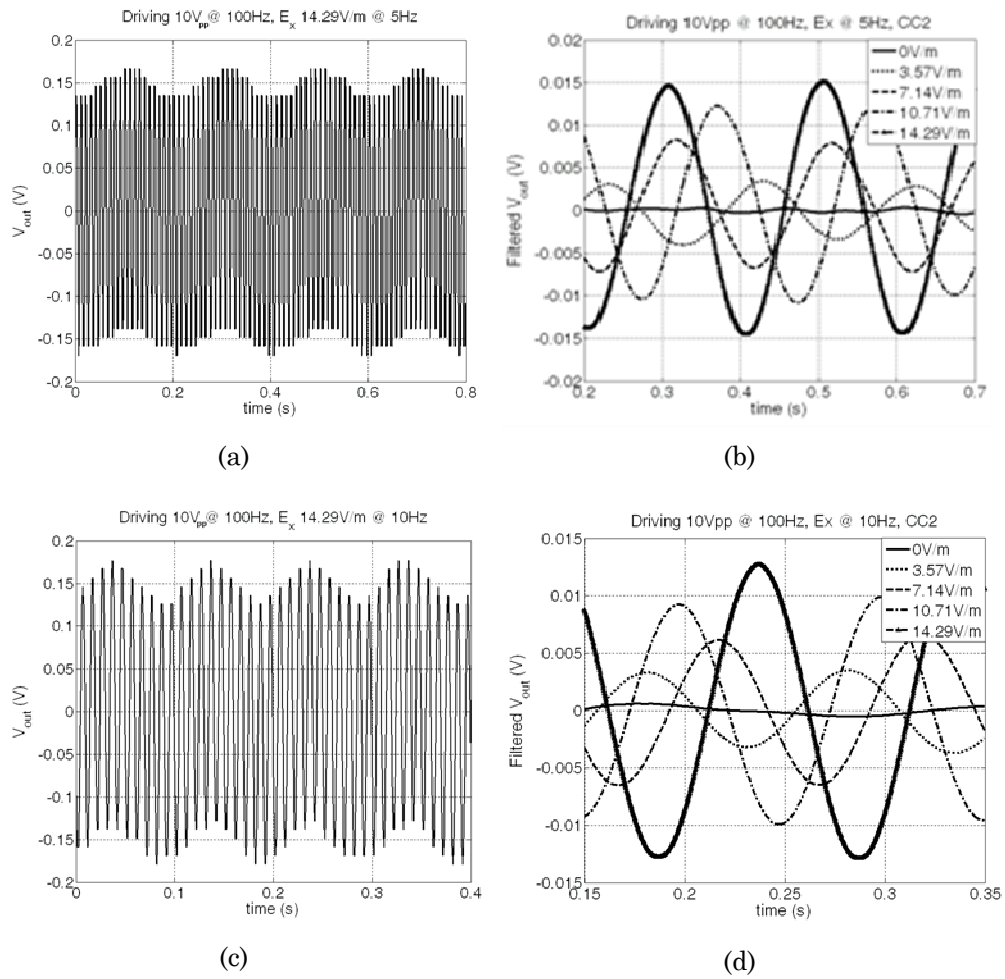| Charge collector dimensions [cm x cm]	Driving amplitude [V]	Driving frequency [Hz]	E-field intensity [V/m]	E-field frequency [Hz]
CC1: 30x39.5			3.57	
CC2: 25.5x25.5	10	100	7.14	5
			10.7	10
CC3: 9x9			14.29	

(a)

(b)

(c)

(d)

FIGURE 4-22   (a) and (c) Sawyer-Tower circuit output signals for driving voltages amplitude of 10 Vpp @ 100 Hz and a target E field of 14.29 V/m @ 5 Hz and 10 Hz respectively; (b) and (d) voltage signals from the ST circuit after low-pass filtering and removal of mean value.
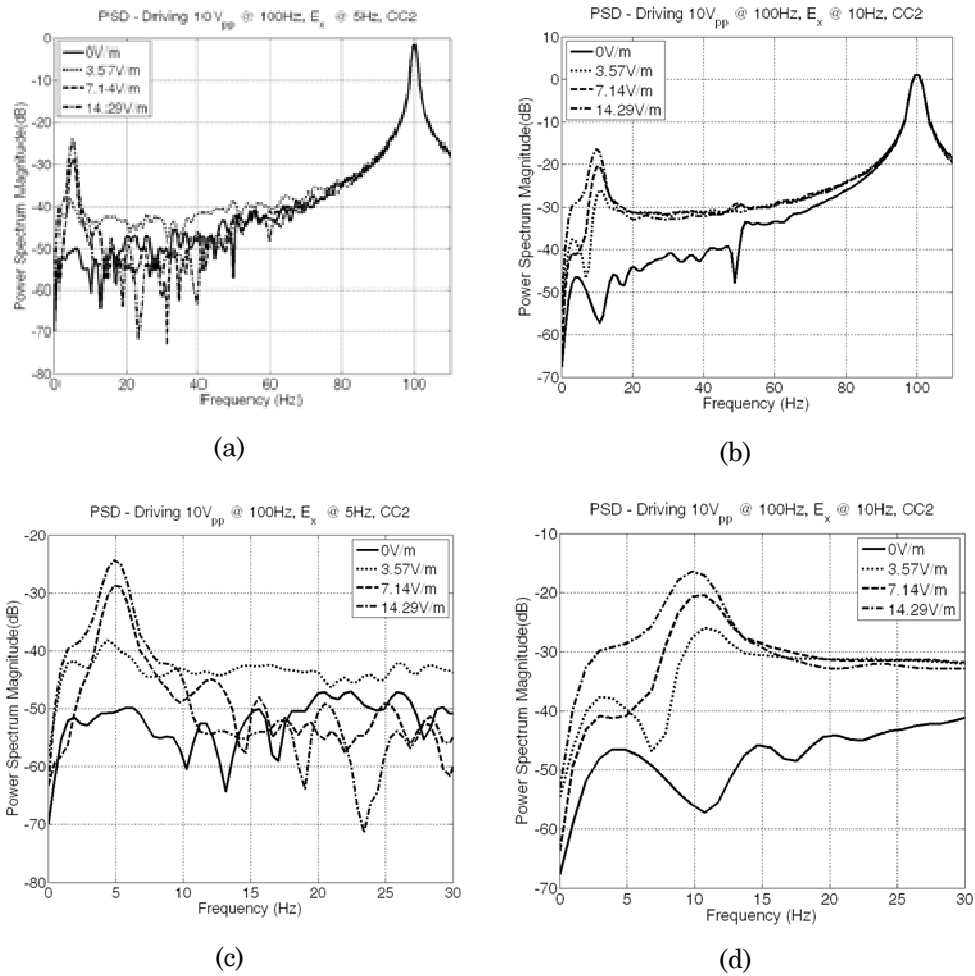
(a)

(b)

(c)

(d)

FIGURE 4-23   Power spectral density plots of the ST output signals for the cases of a driving (i.e. reference) signal of 10 Vpp @100 Hz and a target electric field at 5 Hz (a) and 10 Hz (b). Zooms are given in (c) and (d). The legend on each graph shows the amplitudes of the target electric field.

It is immediately apparent that there might exist an ideal dimension (between CC1 and CC2) for the collector, probably due to saturated operation of the device after a certain value of the charge collector area. Figures 4-24 have two different y-axes scales: on the left, the peak-to-peak output voltage is shown, whereas the normalized (to the

energy barrier height $U_0 = a^2/4b$) filtered polarization is shown on the right axis. Note that the ratio $P/U_0^{1/2}$ is dimensionless.
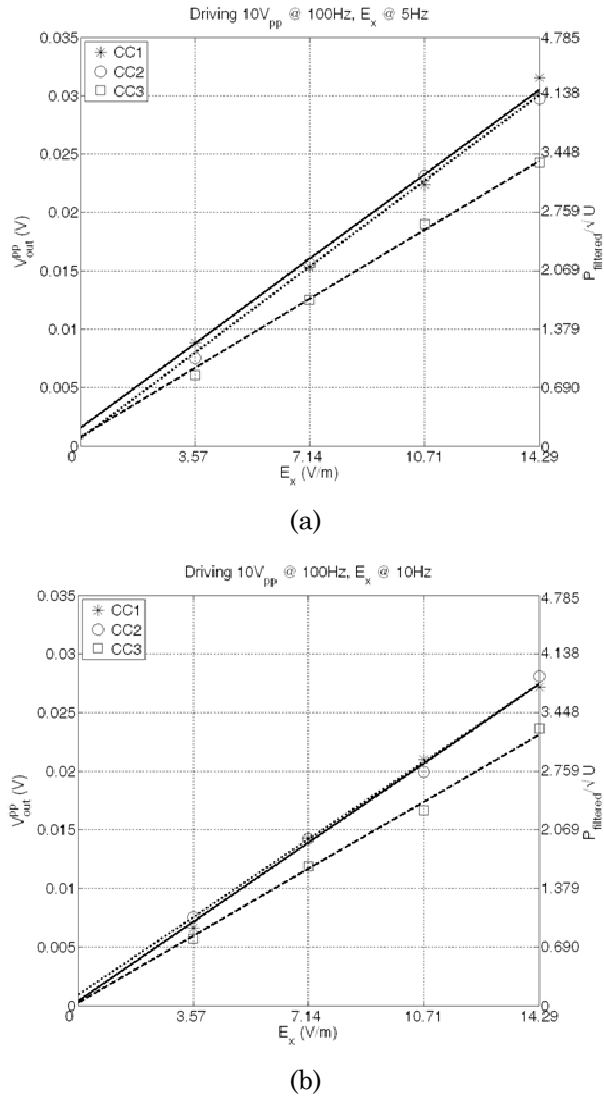

(a)

(b)

FIGURE 4-24   Linear interpolation of the peak-to-peak values of the output signals obtained with the various "charge collectors" and a target electric field having frequency of (a) 5 Hz and (b) 10 Hz. The energy barrier is $U_0 = 5.3812e^{-6}\ C/m^2$

TABLE 4-3   Parameters related to the linear interpolation indicated in
(4.32).

Frequency [Hz]	Charge collector Parameter	CC1	CC2	CC3
5	α [m/V]	7.4e-3	7.5e-3	5.6e-3
	β [V]	2.0e-3	1.6e-3	2.0e-3
10	α [m/V]	5.8e-3	5.6e-3	4.8e-3
	β [V]	2.4e-3	3.5e-3	2.6e-3

While the experimental results demonstrate the ability of the
ferroelectric device to sense quasi-static electric fields, an actual
characterization (via a measure that can be used for comparison
purposes) of the performance remains to be done.

An important performance parameter is the "resolution" which defines
the smallest variation of the measurand that the device can resolve. To
obtain this figure of merit, it is necessary to evaluate the noise floor
through an analysis of the PSD. The results, for the cases of driving
voltages of 10 V_{pp} and 50 V_{pp} and two frequencies (5 Hz and 10 Hz) of
the electric field and for the three charge collectors are reported in
Table 4-4. We note that the best results in terms of low noise (noise
floor) have been obtained with a driving voltage of 10 V_{pp} and a target
field frequency of 10 Hz.

Finally, to conclude this section, the pending problem of demonstrating
the validity of the model (4.13) is addressed. To this end, starting from
the results shown in Figure 4-24, the ratio between the variation of the
polarization P and the variation of the target electric field (this ratio
provides a measure of the device efficiency) as a function of the ratio
between the two areas $S1$ and $S2$ (recall that these are the areas of the
surface of electrodes of the two capacitors shown in Figure 4-6) has been
evaluated for the three charge collectors.

TABLE 4-4   Evaluation of noise floor for two frequencies of the electric field (5 Hz and 10 Hz) and two amplitudes of the driving voltage (10 V_{pp} and 50 V_{pp})

Noise floor [$(V/m)/\sqrt{Hz}$]				
Driving voltage @100Hz [V]	**E-field frequency [Hz]**	**CC1**	**CC2**	**CC3**
10	5	16	0.49	19.8
	10	**0.4**	**0.4**	**0.45**
50	5	5.76	6.67	7.5
	10	3.7	3.4	5.2

The results for the two driving signals of 10 V_{pp} @ 100 Hz and 50 V_{pp} @ 100 Hz are shown in Figure 4-24, and have been interpolated by the following relationship

$$\frac{\Delta P}{\Delta E_x} = \theta_1 \varepsilon_0 \frac{S1}{S2} + \theta_2 \qquad (4.33)$$

where, taking into account the theoretical expressions (4.13), the coefficients θ_1 and θ_2 must to assume values 1 and 0 respectively.

Referring to the experimental data shown in Figure 4-24, the values for θ_1 and θ_2 have been derived via a linear interpolation of the two first points (before then the saturation effects observed for larger plates).

The slopes of the two lines are identical, thus demonstrating the effectiveness of the charge collecting strategy even though the efficiency is lower than what is theoretically predicted (this is probably related to the non-idealities in the experimental prototype). In addition, the effect of the driving signal amplitude is apparent: as expected, the external target electric field can produce a stronger perturbation effect over a lower polarized device and therefore the 10 V_{pp} working condition appears to be the most suitable for the capacitors considered here.
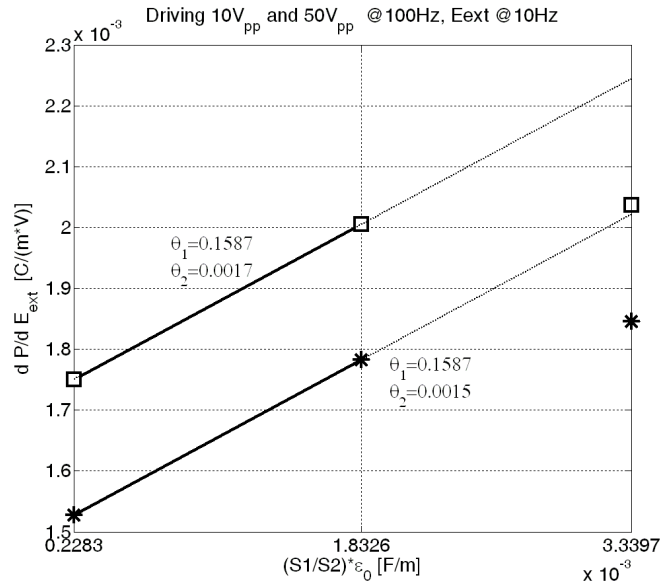
FIGURE 4-25   The ratio between the variation of the polarization P and the variation of the target electric field (this ratio provides a measure of the device efficiency) as a function of the ratio between the two areas $S1$ and $S2$. Square symbols and star symbols are used for a driving signal of 10Vpp@100Hz and 50Vpp@100Hz, respectively. A linear interpolation is also shown as used to estimate parameters θ_1 and θ_2; only the data not affected by saturation have been considered.

Put differently, the target signal is quantified through its modulation of the output waveform, this modulation will be more "visible" if the driving signal is lower; hence the ideal driving signal would have an amplitude just above what is necessary to overcome the coercive field of the material.

5.2   THE RADIANT CAPACITOR

The structure of the capacitor investigated in the previous section aims to mimic the ideal structure presented in Figure 4-4. Nevertheless it has allowed us to confirm experimentally what theory and simulations had predicted.

In the normal progression toward the best suitable configuration a milestone was the one that at the end lead us to design and to place an order to Radiant Technologies Inc. [164] for the manufacturing of the first version of an integrated ferroelectric capacitor with the desiderated structure. This capacitor (the DIEES rel.1 capacitor) will be investigated in the next section. Here the investigation of suitability of capacitors produced by Radiant will be discussed. The main objective was the survey of the technology used by the manufacturer to be ensure it was compatible with our purpose.

To this purpose we purchased from Radiant five packaged dies containing their standard parallel-plate ferroelectric capacitors. These capacitors are made by about 1600 Å of 4/30/70 PNZT and Pt/LSCO electrodes. For both the top and bottom electrodes the LSCO rests between the platinum and the PNZT surfaces. A microscope image of the die with the capacitors in the outer ring (the central part of the die hosts other test structures and it is not of interest for us) together with a schematization of the investigated capacitors are shown in Figure 4-26 (a) and (b), respectively. The size of the capacitors here investigated is 220 μm x 220 μm.

Radiant uses a 5 μm integrated process, with the possibility to yield some features on some layers down to 1 micron [165]. A schematization of the Radiant's technology with the layers' name is shown in Figure 4-27a while a simplified schematization of the same technology with indicated the thickness and the material composition of each layer is given in Figure 4-27b. With reference to Figure 4-27, the substrate used is a 4", 500 μ thick <100> boron doped silicon wafers with a nominal doping level of 10^{15} and with 5000 Angstroms (Å) of thermal silicon dioxide and a little (400 Å) titanium dioxide glue layer (TiOx barrier) under the 1500 Å thick platinum bottom electrodes (BE).
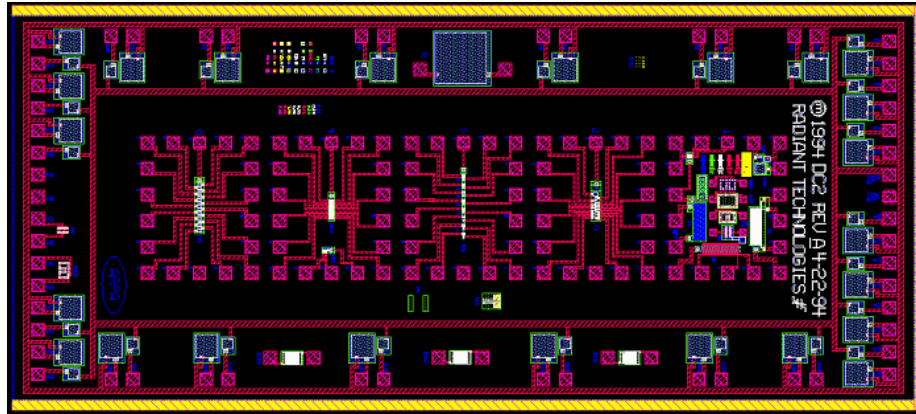
(a)
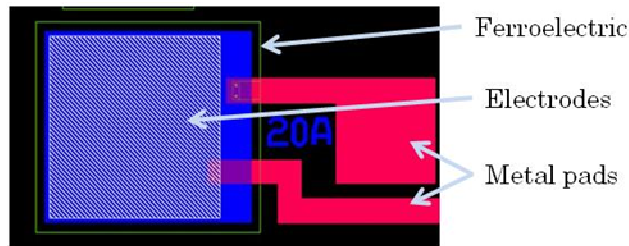
(b)

FIGURE 4-26   (a) A microscope image of the die with the capacitors in the outer ring (the central part of the die hosts other test structures and it is not of interest for us); (b) A schematization of the investigated capacitors. The size of the capacitor is 220µm x 220µm.

A 600 Å Lanthanum strontium cobaltate oxide (LSCO) layer (BO) is interposed between the platinum electrode and the ferroelectric material to improve the bonding between the platinum electrode and the ferroelectric. The ferroelectric (FE) has a composition of 4/30/70 PNZT and a thickness of about 1600 Å. Two layers of LSCO (TO) and platinum (TE) of 600 Å and 1000 Å, respectively, are deposed over the FE to realize the top electrode of the capacitor. All the stack is then covered by a passivation layer of titanium dioxide (400 Å) plus about 2300 Å of S_iO_2 glass (ILD). For the sake of completeness, M1 is the electrical interconnect layer used to form bond pads and connect the electrodes to the bond pads. It consists of 200 Å of Cr with 5000 Å of Au.
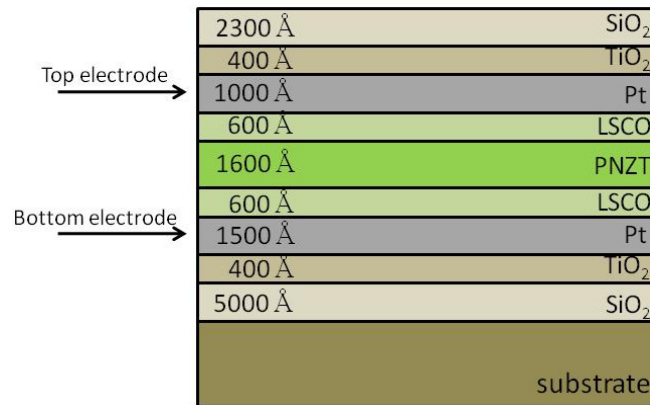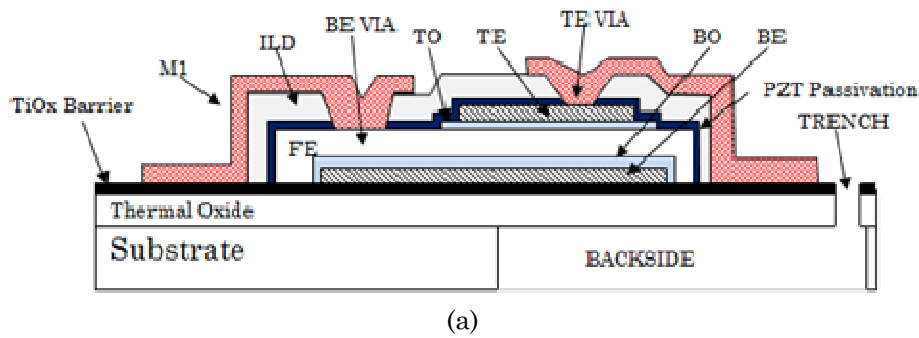
(a)

(b)

FIGURE 4-27   (a) A schematization of the Radiant's technology with the layers name indicated; (b) A simplified schematization of the same technology with indicated the thickness and the material used for each layer.

5.2.1 STRUCTURAL MODIFICATION

With the purpose to use the ferroelectric capacitor to sense electric fields exploiting our methodology a modification on the top electrode to obtain a third separated electrode by which to perturb the polarization state of the device was needed. A schematization of the new configuration together with an example of dimensions is presented in Figure 4-28.

The modification consists in to remove a ring from the top electrode to release a central plate (the sensing electrode) electrically isolated from

the outer part of the top electrode. The sensing electrode will be linked to an external plate to collect the electric charges induced by the external target electric field.
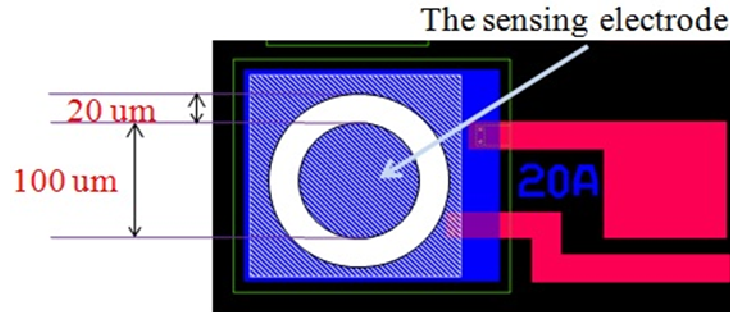

FIGURE 4-28   Schematization of the structural modification of the top electrode of the capacitor needed to realize the sensing electrode.
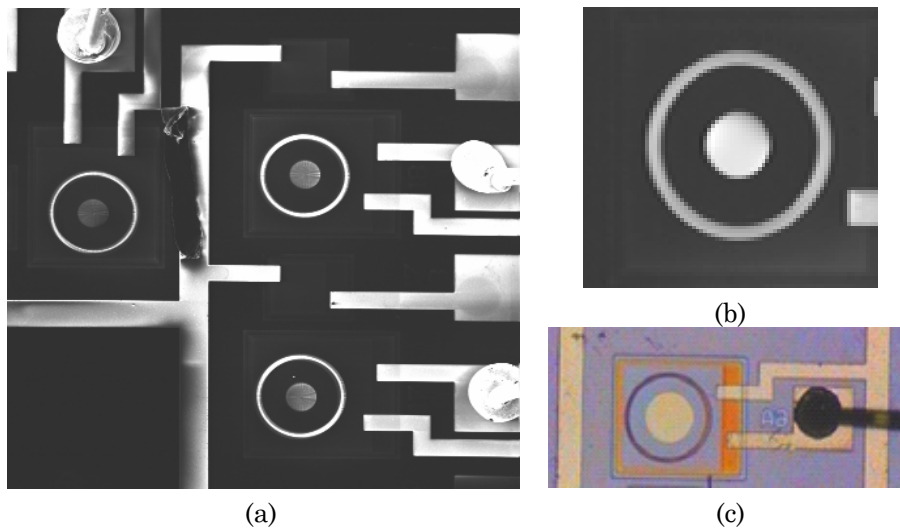

FIGURE 4-29   Ferroelectric capacitors produced by Radiant Technologies after the modification by the FIB of the top electrode. (a) three modified capacitors; (b) and (c) zoom of a single capacitor. The disc in the central part of the sensing electrode is the zone in which the passivation has been removed to the purpose to electrically contact the electrode.

The removal of the ring (passivation, platinum and LSCO) from the top electrode has been performed by a Focused Ion Beam (FIB) by kind permission of STMicroelectronics in Catania and in particular by the courtesy and collaboration of Dr. La Mantia and his staff.

Figure 4-29 shows FIB images of the ferroelectric capacitors produced by Radiant Technologies after the modification of the top electrode. Figure 4-29a shows three modified capacitors while a zoom of a single capacitor is shown in Figures 4-29 (b) and (c). The disc in the central part of the sensing electrode represents the zone of the sensing electrode in which the passivation has been removed to enable us to contact the electrode.

5.2.2   EXPERIMENTAL RESULTS

To start, a wide and detailed characterization of the behavior of all the ferroelectric capacitors in the P-E domain for various amplitudes and frequencies of the driving voltage, applied between the bottom and the outer top electrodes have been carried out. The ST circuit discussed in section 3.1 has been used to convert the ferroelectric polarization in a proportional output voltage signal. The electronic implementing the ST circuit together with the DIP-28 package hosting the ferroelectric capacitors is shown in Figure 4-30. Data acquisitions have been then elaborated by the identification tool introduced in section 5.1.3 adopting even for these capacitors the dynamic model (4.8) to describe their dynamic behavior.

Figure 4-31 shows some examples of experimental P-E hysteresis (red line) for the capacitor C6 of the package 2 for three amplitudes of the driving voltage ($14V_{pp}$, $8V_{pp}$ and 5 V_{pp}) and two different frequencies (70 kHz and 10 kHz) together with the hysteresis predicted by the model (4.8) with the identified parameters (blu dotted line).

As an example, in Table 4-5 the parameters identified for the same capacitor for different amplitudes and frequencies of the driving voltage, are reported. Furthermore, the value of the root mean square type functional J that computes (as a percentage) the residuals between the predicted (via the model) values and the observed values of the polariza-
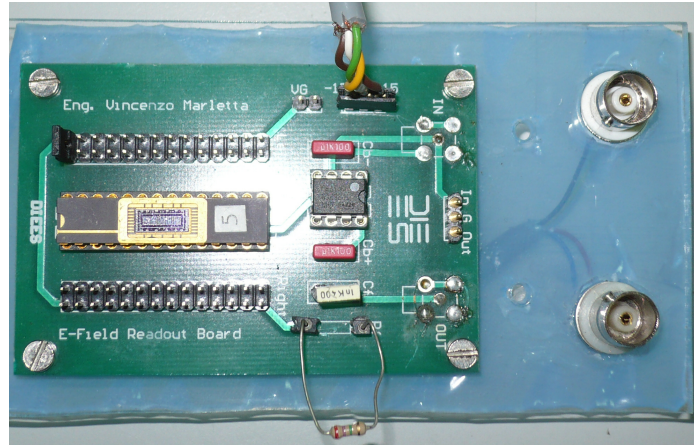
FIGURE 4-30   The electronic implementing the Sawyer-Tower circuit together with the DIP-28 package hosting the ferroelectric capacitors fabricated by Radiant Technologies Inc.

tion, together with the values of the error defined as the root square residuals, have been included.

Finally the value of the remnant polarizations evaluated by the experimental hysteresis are reported in the last right column.

The same procedure has been adopted for all the others capacitors and for the sake of brevity their related hysteresis and identified parameters will not reported here.

Driving 14 V$_{pp}$

70 kHz   10 kHz

Driving 8 V$_{pp}$

70 kHz   10 kHz

Driving 5 V$_{pp}$

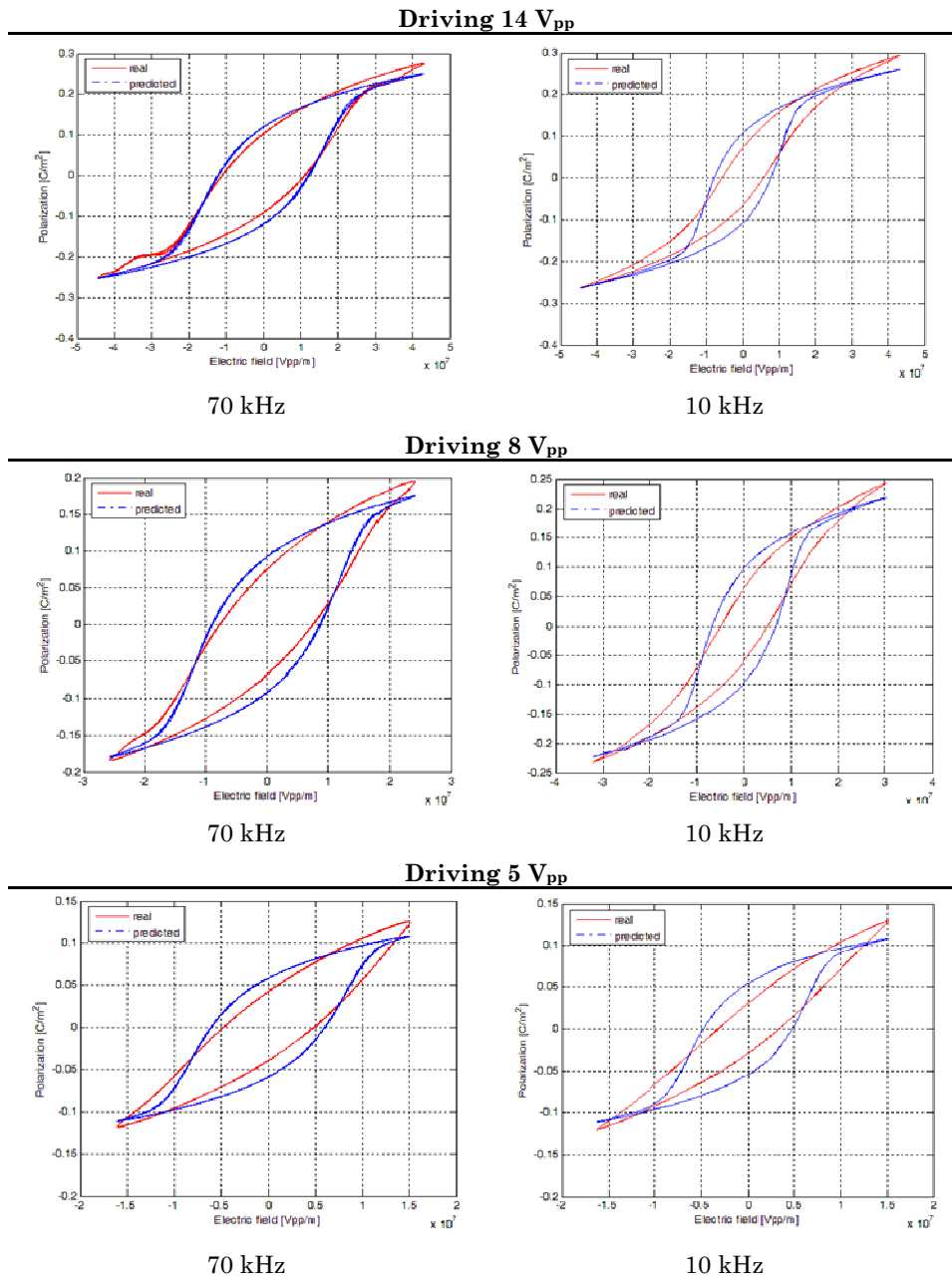70 kHz   10 kHz

FIGURE 4-31   Examples of experimental P-E hysteresis (red line) for three amplitudes and two frequencies of the driving voltage together with the hysteresis predicted by the model (4.8) with the identified parameters (blu dotted line).

TABLE 4-5   The parameters identified for the capacitor C6 of the package 2 for different amplitudes and frequencies of the driving voltage.

Parameters Identified for the capacitor C6 of the Package 2

| Frequency	a	b	c	τ	J	error	P_r
Driving 14 V$_{pp}$							
70kHz	6.269e-14	1.803e-3	6.570e-13	2.814e-11	7.936	4.955e-1	0.097
60kHz	6.317e-14	1.721e-3	6.228e-13	2.814e-11	8.651	5.397e-1	0.185
50kHz	6.003e-14	1.610e-3	5.727e-13	2.814e-11	9.232	5.748e-1	0.088
40kHz	6.809e-14	1.456e-3	5.066e-13	2.814e-11	10.007	6.198e-1	0.083
30kHz	7.589e-14	1.282e-3	4.238e-13	2.814e-11	11.159	6.798e-1	0.074
20kHz	5.871e-14	9.146e-4	3.117e-13	2.814e-11	11.215	6.941e-1	0.071
10kHz	4.898e-14	5.212e-4	1.754e-13	2.814e-11	12.279	7.589e-1	0.064
Driving 12 V$_{pp}$							
70kHz	6.284e-14	1.881e-3	6.307e-13	2.814e-11	7.445	4.275e-1	0.092
60kHz	5.613e-14	1.791e-3	5.943e-13	2.814e-11	8.172	4.696e-1	0.087
50kHz	5.384e-14	1.659e-3	5.407e-13	2.814e-11	8.723	4.995e-1	0.083
40kHz	5.335e-14	1.479e-3	4.760e-13	2.814e-11	9.502	5.440e-1	0.077
30kHz	4.968e-14	1.254e-3	3.934e-13	2.814e-11	10.162	5.761e-1	0.073
20kHz	4.567e-14	9.270e-4	2.899e-13	2.814e-11	10.514	5.988e-1	0.068
10kHz	4.070e-14	5.287e-4	1.639e-13	2.814e-11	11.466	6.533e-1	0.061
Driving 10 V$_{pp}$							
70kHz	6.246e-14	2.033e-3	5.933e-13	2.814e-11	8.042	4.137e-1	0.083
60kHz	5.830e-14	1.943e-3	5.568e-13	2.814e-11	8.917	4.570e-1	0.079
50kHz	5.780e-14	1.761e-3	4.996e-13	2.814e-11	9.360	4.799e-1	0.076
40kHz	5.668e-14	1.575e-3	4.377e-13	2.814e-11	10.154	5.181e-1	0.071
30kHz	5.575e-14	1.301e-3	3.598e-13	2.814e-11	10.623	5.447e-1	0.067
20kHz	5.107e-14	9.543e-4	2.615e-13	2.814e-11	10.944	5.597e-1	0.064
10kHz	4.186e-14	5.457e-4	1.490e-13	2.814e-11	11.965	6.131e-1	0.057

TABLE 4-5 (continue)   The parameters identified for the capacitor C6 of
                              the package 2 for different amplitudes and
   frequencies of the driving voltage.

(continue) Parameters Identified for the capacitor C6 of the Package 2

| Frequency	a	b	c	τ	J	error	P_r
			Driving 8 V$_{pp}$				
70kHz	6.109e-14	2.419e-3	5.452e-13	2.814e-11	9.575	4.181e-1	0.072
60kHz	5.932e-14	2.297e-3	5.079e-13	2.814e-11	10.473	4.563e-1	0.068
50kHz	5.906e-14	2.052e-3	4.504e-13	2.814e-11	10.772	4.690e-1	0.065
40kHz	6.285e-14	1.822e-3	3.920e-13	2.814e-11	11.605	5.032e-1	0.061
30kHz	7.114e-14	1.484e-3	3.197e-13	2.814e-11	12.092	5.254e-1	0.058
20kHz	7.792e-14	1.064e-3	2.297e-13	2.814e-11	12.132	5.304e-1	0.056
10kHz	8.580e-14	5.960e-4	1.301e-13	2.814e-11	13.2482	5.839e-1	0.050
			Driving 5 V$_{pp}$				
70kHz	9.752e-14	5.437e-3	4.653e-13	2.814e-11	13.773	3.705e-1	0.041
60kHz	9.942e-14	5.133e-3	4.265e-13	2.814e-11	14.256	3.823e-1	0.038
50kHz	1.073e-13	4.413e-3	3.734e-13	2.814e-11	14.420	3.898e-1	0.038
40kHZ	1.106e-13	3.959e-3	3.235e-13	2.814e-11	14.913	4.006e-1	0.035
30kHz	1.134e-13	3.120e-3	2.581e-13	2.814e-11	15.110	4.099e-1	0.033
20kHz	1.362e-13	2.127e-3	1.823e-13	2.814e-11	15.294	4.190e-1	0.033
10kHz	1.028e-13	1.183e-3	1.009e-13	2.814e-11	16.359	4.497e-1	0.030

With the purpose to demonstrate the possibility to exploit the
ferroelectric capacitors to sense electric fields experiments with the
modified capacitors have been performed applying a potential to the
sensing electrode. To this aim a micro-tip has been used to contact the
sensing electrode. Figure 4-32 show the setup used for the experiments
and an example of the ST output voltage signal on the oscilloscope. The
ferroelectric capacitor together with the conditioning electronic has been
placed under the microscope with the aim to contact the sensing
electrode (Figure 4-32a) by the micro-tip. Figure 4-32b shows a zoom of
the ferroelectric capacitor with the tip contacting the sensing electrode
obtained by a CCD camera mounted on the optics of the microscope.
A voltage signal produced by a voltage generator is then applied to the
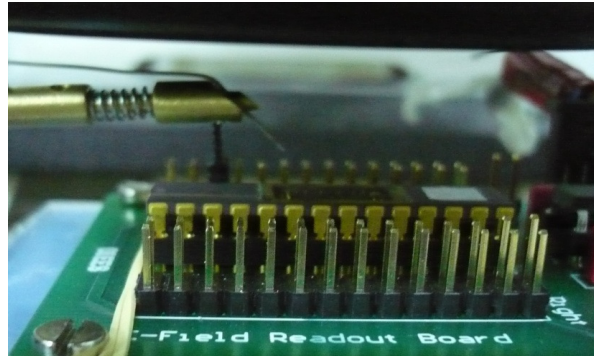
(a)
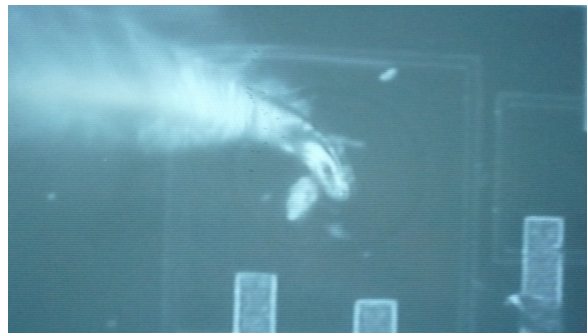
(b)
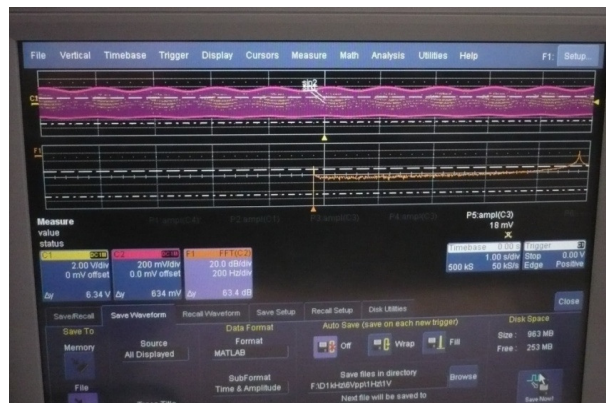
(c)

FIGURE 4-32   (a) The ferroelectric capacitor with the ST circuit under the microscope to contact the sensing electrode by a micro-tip; (b) A microscope image showing the capacitor and the tip contacting the sensing electrode; (c) An example of perturbed ST output voltage after applying a potential to the tip.